

Open Source, In-situ, Intermediate Strain-Rate Tensile Impact Device for Soft Materials and Cell Culture Systems

L. Summey¹ · J. Zhang¹ · A.K. Landauer² · J. Sergay³ · J. Yang⁴ · A. Daul¹ · J. Tao¹ · J. Park¹ · A. McGhee¹ · C. Franck^{1*}

Received: date / Accepted: date

Abstract

Background: Intermediate-strain-rate mechanical testing of soft and biological materials is important when designing, measuring, predicting, or manipulating an object or system's response to common impact scenarios. Open source micro-mechanical test instruments that provide high spatial and temporal resolution volumetric strain field measurements, non-destructive testing and gripping of soft materials with low elastic moduli, programmable strain rates spanning from 10^{-6} s^{-1} to 10^2 s^{-1} , and biocompatibility for living cell cultures and tissues in one instrument are lacking in the current literature.

Methods: We introduce a micro-tensile testing device developed to meet all these criteria while being straightforwardly accessible to the end user. This device sits atop an inverted microscope stage, granting the researcher access to 3D spatial resolutions as low as 100 nm and frame rates only limited by the camera speed and availability of recordable photons. The micro-tensile specimen is attached to the test device by a specially designed fixture. This enables a material to be cast into the mold assembly and tested without being manually manipulated before or after testing. The tensile deformation is controlled by two voice-coil linear actuators synchronized to pull a specimen in opposing directions. A field of view focused centrally on the specimen experiences a highly-controllable uniform tensile strain with minimal rigid body motion.

Results: We validate the resulting in-plane strain fields on a 2D poly-dimethylsiloxane (PDMS) substrate and a heterogeneous polyurethane foam using Digital Image Correlation (DIC) and volumetrically on 3D polyacrylamide (PA) hydrogels using Digital Volume Correlation (DVC). High-Rate Volumetric Particle Tracking Microscopy (HR-VPTM) is used to quantify and validate the 3D volumetric strain fields at impact-relevant rates. The device can apply up to 200 % engineering strain with peak strain rate up to approximately 240 s^{-1} to a 7 mm long dogbone specimen. Proof-of-concept biocompatibility was tested on 2D and 3D *in vitro* neural cell cultures, demonstrating the versatility and applicability for both soft materials and living biomaterials.

Conclusion: We demonstrate and validate a versatile micro-tensile impact device for soft materials and *in vitro* cellular biomechanics investigations. The achievable strain rates for such a design are some of the highest we have found reported to date and enable experiments that replicate the full range of observable large material deformations seen during real-world blunt impacts.

Keywords In vitro Tension Device · High-Speed 3D Imaging · Intermediate Strain Rate · Neural Cell Culture · Digital Image Correlation · Digital Volume Correlation · Micro-Tensile Testing

1 Introduction

Characterization of living and non-living soft material systems requires unique measurement tools and instruments that are distinct from traditional means of material characterization [1–5]. That is, tissue and complex polymeric soft materials feature innate micro-structural heterogeneities and environmental dependencies (e.g., hydration, pH level, temperature) that are often negligible for traditional engineering materials. As complete descriptions of

¹Department of Mechanical Engineering, University of Wisconsin-Madison, Madison, WI, USA 53706

²National Institute of Standards and Technology, Material Measurement Laboratory, 100 Bureau Drive, Gaithersburg, MD, USA 20899

³Department of Biomedical Engineering, University of Wisconsin-Madison, Madison, WI, USA 53706

⁴Department of Aerospace Engineering & Engineering Mechanics, The University of Texas at Austin, Austin, TX, USA 78712

*E-mail: cfranck@wisc.edu

material mechanics for these materials require accurate determination of spatiotemporally varying strains at the micrometer-scale, mechanical testing apparatus should support measurement techniques for full field deformations with sub-micrometer imaging resolution. This type of *in-situ* microscopy-based deformation tracking can be integrated with a number of optical microscopy modalities including brightfield, epifluorescence, and confocal imaging [6–10]. These methods have largely focused on applying quasi-static to low strain rate (10^{-6} to 10^{-1} s^{-1}) deformations, often with interrupted loading schemes to account for material relaxation and imaging times. Yet, for replicating tensile impact-like dynamics (i.e., non-constant strain rate during a uniaxial stress experiment with peak rates of $100 s^{-1}$ or more), high-rate testing and real-time deformation measurement are critical for understanding the material behavior and biological responses. In particular, in blunt trauma injury due to impact, tissue strain rates have been estimated to be in the intermediate strain rate regime [11, 12], i.e., strain rates of $1 s^{-1}$ to $250 s^{-1}$. Few devices have been reported capable of delivering controlled impact-rate kinematics in tension, compression or shear dominated loading, while providing full spatiotemporal imaging access in both two and three-dimensions, particularly at the micro-scale. [9, 13, 14] Screw or piezo-driven actuators typically do not have sufficient range in both speed and amplitude for *in-situ* microscopy testing with large deformations at intermediate strain rates. By constraining the device to soft material testing, i.e., elastic moduli less than approximately 1 MPa, we can use precision high-rate, low-force voice coil-type linear actuators to deform the material without exceeding peak load limitations. In addition, most traditional devices are best used with materials that can be fixtured via clamping without damaging the specimen or affecting the total applied strain in the gauge section. Soft materials, such as hydrogels, foams, and living tissues, may be permanently deformed or damaged when even small loads are applied. The clamping force required to adequately grip a specimen often causes unintentional multiaxial states of strain in the gauge section. Thus, it is also important that device’s specimen fixturing technique is designed, and test specimens are fabricated, to avoid detrimental clamping forces.

Here, we describe a novel apparatus specifically designed to accurately administer rapid, large-strain, and high-strain-rate, yet overall low-force tensile deformations thanks to the high compliance of the soft material. This is not merely applicable to soft solids but also extends to living biological systems, thus offering a unique array of test capabilities. Quasi-static tension devices have addressed many of the aforementioned constraints [15–20], but our device expands these capabilities to the intermediate strain-rate regime for micro-tensile specimens while including customization options for maximum material compatibility. The device itself is comprised of high-rate actuators, an alignment stage and fixturing method, and a novel specimen fabrication and installation process that mitigates fixture-induced measurement aberrations. See Fig. 1 for an overview of the device. It is designed as a stage-top module for *in-situ* microscopy, for full field measurement of the applied deformation, but can be used as a standalone device. Example applications of this device and test method are illustrated using polydimethylsiloxane (PDMS), polyacrylamide (PA), collagen-I hydrogels, elastomeric open-cell foams, and PDMS substrates with attached primary cell cultures, with instructions for adapting the protocol to other soft material. To further demonstrate the breadth of applicability of the device, materials were tested using various methods of displacement and strain field measurement, such as quasi-static Digital Volume Correlation (DVC), 2D high speed Digital Image Correlation (DIC), and 3D High Rate Volumetric Particle Tracking Microscopy (HR-VPTM), as appropriate for their application.

In summary, we present a new open-source device design that can subject soft materials, including living biological systems, to controlled tensile impacts over a broad range of engineering strains ($O(1)$ % to $O(200)$ %) and strain rates (ca. $10^{-6} s^{-1}$ to a peak rate of approximately $240 s^{-1}$ during variable-rate testing). Real-world blunt impacts cause tissues and protective materials to deform at the upper range of these strain rate capabilities ($1 s^{-1}$ to $100 s^{-1}$), where deformation mechanisms and failure mechanics can deviate significantly from quasi-static and low-speed behaviors [11, 21–25]. To this end, this test device emulates impact-like conditions in a controllable, measurable way for a micro-tensile specimen, which is an important step forward in understanding deformation, damage, and injury mechanics. We begin with an introduction to the micro-tensile impact apparatus, accompanied by an examination of several specimen creation methodologies and their corresponding fixturing procedures applicable to a variety of soft materials. Subsequently, we present an array of experiments for validation and demonstration purposes. We include scripts, solid models, and parts list of the necessary components to fabricate this device with comments to encourage customization for new applications.

2 Experimental Methods

2.1 Micro-Tensile Impact Device Design and Operation

The device (Fig. 1) is custom-fitted to a baseplate for a Nikon Ti2 inverted microscope motorized x_1 - x_2 stage, although this can be readily changed to match any inverted microscope stage. The core device to impose tension-dominated deformation on the specimen consisted of a pair of horizontally opposed, coaxial linear voice coil

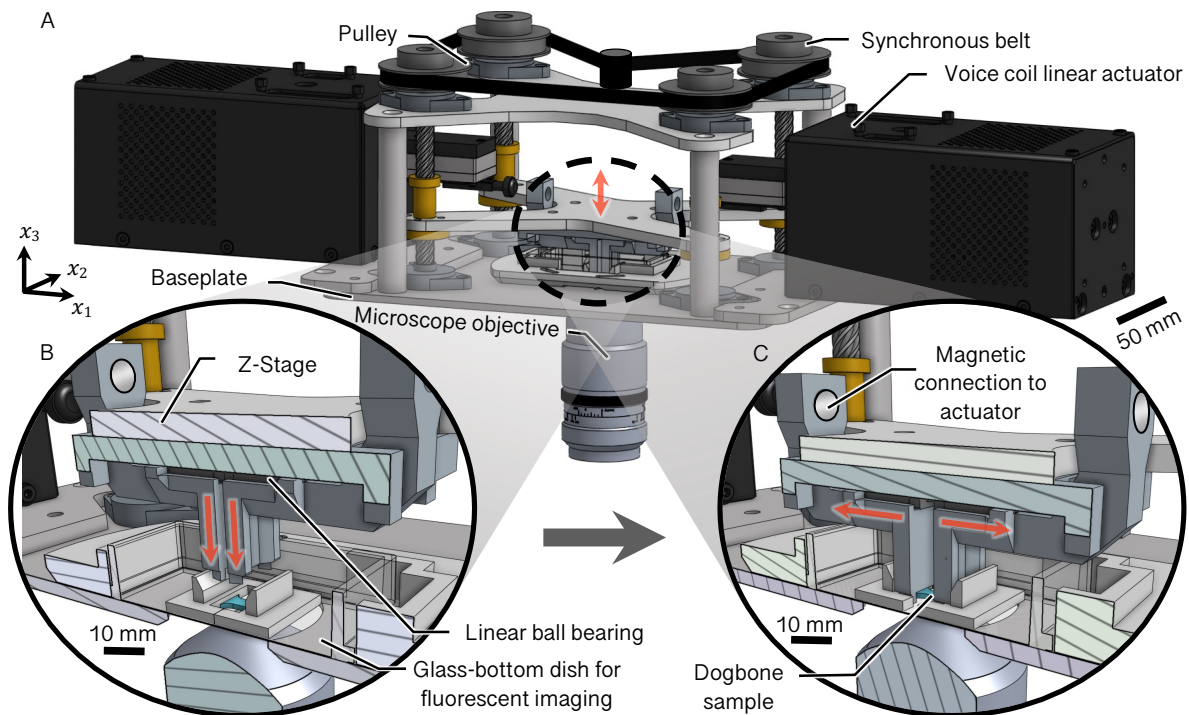


Fig. 1 Illustration of the complete device, whose baseplate is designed to be mounted into the motorized stage of an inverted microscope. (A) A synchronous belt and pulley system rotate four lead screws to precisely control the vertical position of the z-stage containing the horizontal-motion-control assembly. (B) The z-stage assembly before it contacts the prepared dogbone specimen. The specimen sits in the center of a glass bottom dish that is compatible with most inverted microscope imaging systems. (C) When the z-stage is lowered, the device contacts the grippers of the dogbone specimen. The two components that contact the grippers slide independently using linear ball bearings moving on the same stainless steel rail. This sliding motion is controlled by the two voice coil actuators to apply a prescribed displacement to the dogbone specimen.

actuators (Physik Instrumente V-277.631) mounted on a rigid frame. To control the vertical (x_3 -direction) position of the contact points between the device and the specimen fixture, a synchronous belt and pulley system turns four lead screws mounted to a vertical motion “Z-stage” containing a horizontal-motion-control assembly. This assembly holds a stainless steel rail with two co-linear ball bearings. Mounted to each of these bearings are custom 3D printed “fingers” with strong neodymium rare earth magnets placed such that the magnets attach directly to their respective voice coil linear actuators when the z-stage is lowered into place on one end, and which extend downward to engage with the top of the specimen fixtures at the other end. This creates a direct connection from the actuators to the specimen fixture through four triangular, self-aligning touch points. The center of the baseplate is removed to allow for simultaneous microscopy imaging of the stretched specimen. The objective lens can be brought into contact with the glass bottom of the specimen dish for water- and oil-imaging as needed. The specimen is stretched when the fingers are separated by the translation of their respective actuators, while the bearings practically eliminate any applied moments and constrain the specimen fixture to uniaxial motion along the primary tension direction (the x_1 -direction). We chose two voice coil linear actuators to effectively double the maximum strain and strain rates experienced by the specimen, and to ensure symmetric stretch along the x_1 -direction about the center of the specimen (Fig. 1B,C). This is crucial for high-resolution large deformation measurements, as high magnification imaging objectives yield small fields of view, and local deformations tracked for large strain magnitudes would be quickly lost within the fixed camera field of view due to large rigid body motion effects away from the stationary point of the deformation.

When initially programming the device to achieve a desired strain magnitude, displacements were estimated by calculating the engineering strain at the center of the material. The programmed strain and strain rate were defined from uniaxial displacement of the actuators as

$$\varepsilon = \Delta L / L_0, \quad (1)$$

$$\dot{\varepsilon} = \partial \varepsilon / \partial t. \quad (2)$$

ΔL was the combined displacement of both linear actuators, L_0 was the undeformed gauge length (Fig. 2) of the specimen (approximately 7 mm), and t was the test time. The displacements of both linear actuators were synchronized by programming two *Physik Instrumente C-413* controllers with the desired triangular displacement-time profile, and triggering them with a common Transistor-Transistor Logic (TTL) signal. An iterative adjustment

of the programmed displacement of the actuators is used to match the measured, spatially-averaged axial Lagrange strain (E_{11}) of the specimen to the target value for the experiment, as a calibration step. The local Lagrange strain tensor (\mathbf{E}) is measured using the methods in section 3, where the Lagrange strain tensor is defined as

$$\mathbf{E} = 1/2 (\mathbf{F}^T \mathbf{F} - \mathbf{I}), \quad (3)$$

with \mathbf{F} being the measured local deformation gradient tensor, $(\cdot)^T$ the transpose operator, and \mathbf{I} the identity tensor. This is defined in either a 2D or 3D basis space depending whether 2D or 3D measurements are used to compute the deformations. To achieve a specific target strain and strain rate, the programmed strain pulse was iteratively adjusted for each new material to account for stiffness differences and any peculiarities within the specimen geometry or boundary conditions, with a new test specimen used after calibration. These effects can cause the measured local strains to be substantially different than the programmed target applied strain, and thus direct full-field measurements are critical to ensure fidelity of the experiment.

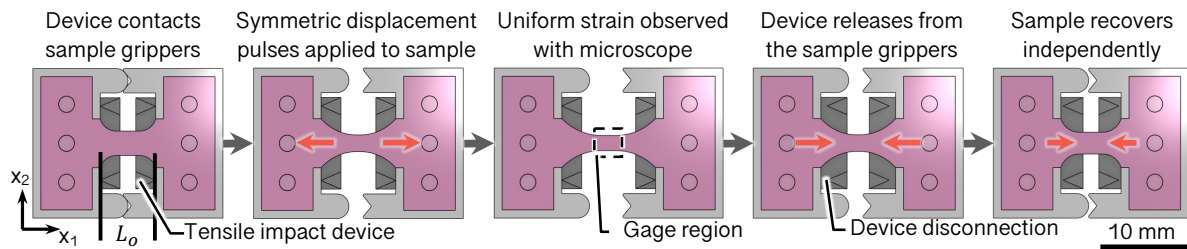


Fig. 2 Illustration of the dogbone specimen and gripper assembly as viewed from below. The various stages of movement during a typical experiment proceed from left to right. Two halves of the fixture start in contact with each other while the specimen is cured in place. When the fixture is pulled apart by the device, the specimen experiences simple tension in both the positive and negative x_1 -direction. The device disconnects from fixture to allow the specimen to freely relax, but it is possible to drive the fixture back to the originally zero-strain configuration with minor adjustments to the connection components.

2.2 Fabrication of Micro-Tensile Test Specimens

Materials such as collagen-I, alginate, agarose, and polyacrylamide (PA) hydrogels are difficult to manipulate without damage, so polymerizing them directly into a chemically functionalized fixturing apparatus is a preferred method for these material. Previous tensile impact devices compatible with *in vitro* cell culture typically employ 2D flexible membranes as the substrate for growing cells, and are secured in place after a substrate of cells are cultured [9, 15, 20, 26–28]. This limitation means that only materials that can withstand manual clamping can be tested (poly(dimethylsiloxane), silicone, etc.). We combined this concept with dogbone tensile specimens typical of uniaxial tensile testing [26, 29–33]. The fixture was designed to hold the gauge portion of the material at constant length until intentionally separated by the device even when disconnected from the device. The method for fabricating dogbone test specimens varies depending on the application. In an effort to generalize this device for use with a variety of soft materials, the specimen fixture was customized with limited adjustments when necessary. The fixture, which consists of two grippers and a support or mold that press-fit together, was additively manufactured using FormLabs Biomed Clear resin on a Form3B stereolithographic (SLA) 3D printer (Formlabs, Somerville, MA)¹. This material is stable over a wide range of pH and therefore allows for pH dependent gelation of various hydrogels. The printed fixtures were post-processed using the manufacturer recommended one hour cure cycle under ultraviolet (UV) light at approximately 60 °C. For PDMS and adhesives to cure to the surface of the resin, and to promote biocompatibility, we found that it was also necessary to immerse the fixture in an Isopropyl Alcohol (IPA) bath for at least four hours and autoclave them using the gravity cycle for one hour. To functionalize the 3D printed specimen fixture, we adapted a previously described hydrophilic (aminosilanized) glass coverslip procedure [34] by increasing the concentration of (3-aminopropyl)trimethoxysilane (APTMS) in ethanol from 0.5 % v/v to 2 % v/v for 20 minutes. Following a thorough rinse in nominally 100 % ethanol, we soaked the coated fixture in an 8 % glutaraldehyde by volume mixture in water. This encouraged specimen attachment to the fixture surfaces (e.g., in the final steps shown in Fig. 3). The functionalization steps may not be possible if using alternative 3D print materials to fabricate the fixture, but the device was adaptable to most soft material with minor adjustment

¹ Certain commercial equipment, instruments, or materials are identified in this paper in order to specify the experimental procedure adequately. Such identification is not intended to imply recommendation or endorsement by NIST, nor is it intended to imply that the materials or equipment identified are necessarily the best available for the purpose.

and troubleshooting. We successfully tested the device under three conditions typical of a broad range of testing requirements.

2.2.1 Fabrication of Nominally-2D Specimens

To create a substrate compatible with the tension device for 2D *in vitro* cell cultures, PDMS was cast into a flat, thin dogbone shape (Fig. 3A). The dogbone template mold was fabricated via soft photolithography. A photoresist polymer (SU-8 100, MicroChe, Westborough, MA) was spun coat to approximately 250 μm atop a nominally 101.6 mm (4 in) silicon wafer (University wafer, Boston, MA). All photolithography preparation, bake, and development steps followed the manufacturer-recommended protocols. Temperatures were gradually ramped (nominally 5 $^{\circ}\text{C}$ per minute) to the target values using a controlled hot plate (TC-720, TE Technology, Traverse City, MI). The dogbone template was patterned on the photoresist using a micro-patterning attachment (Primo module, Alvéole, Paris, FR) to a widefield microscope (Nikon Ti-2 Eclipse, Nikon Instruments Inc., Melville, NY). The wafer was exposed to a nominal 8 mJ/mm^2 UV dose through a 4 \times objective with an exposure time of about 100 ms. Once properly developed, the wafer was silanized with (Tridecafluoro-1,1,2,2-tetrahydrooctyl)trichlorosilane (Gelest, Morrisville, PA) via vapor deposition using a vacuum desiccator to prevent the adherence of PDMS to the wafer.

PDMS is a two-part crosslinked elastomer with tunable mechanical properties, often used for molding, biological substrates, and electronics assemblies. The dogbone specimens were created by distributing a measured volume of base polymer mixture (10:1 volume ratio of A and B parts; SYLGARD 184, Krayden, Denver, CO) into the substrate mold and heating the wafer to approximately 80 $^{\circ}\text{C}$ for approximately 15 minutes. The cured dogbones were peeled from the mold and adhered to a functionalized (O_2 -plasma-treated) specimen fixture with an 80:20 volume ratio mixture of SYLGARD 184 (10:1 volume ratio) to SYLGARD 527 (20:1 volume ratio or prepolymer to crosslinker) as an adhesive. The assembled dogbone specimens were then fully cured at approximately 60 $^{\circ}\text{C}$ overnight (8+ hours). The resulting thickness of the dogbone is 250 μm - 300 μm .

2.2.2 Generation of Die-Cut Specimens

Some soft materials, for example commercially-sourced open-cell elastomeric impact protection foams, can not be molded using the aforementioned methods since it is provided as-is in sheet or bulk form by a manufacturer. Such specimens can be cut into the appropriate shape using a 3D printed dogbone-shaped die cutter (Fig. 3B), or could be laser or waterjet cut if needed. Here, we tested this method using a ca. 1 mm thick slice of elastomeric, open cell impact protection foam (Poron XRD, Rogers Corp, Rogers, CT) with mean cell diameter approximately 70 μm . Due to the comparatively small mean cell diameter (10 times or more smaller) and the die geometry, the inhomogeneity magnitude on the cut edge of the prepared specimen is considerably smaller than the gauge width. The specimen was then glued to the fixture using cyanoacrylate and was placed in a dish; ready to be tested in the device. The foam exhibits significant viscoelasticity, so the material was allowed to freely recover to the undeformed condition for 30 minutes or more prior to testing.

2.2.3 Fabrication of 3D Hydrogel Specimens

This component of the study tested the functionality of the device using polyacrylamide (PA) hydrogels. PA has a highly controllable stiffness and exhibits a nearly perfect neo-Hookean constitutive behavior at low strain rates [35, 36]. The hydrogels were prepared using existing protocols [37] with a concentration of acrylamide to bis-acrylamide solution (Bio-Rad Laboratories, Hercules, CA) of nominally 10% and 0.06% by volume respectively and chemical cross-linking catalysts of 1.25% ammonium persulfate (APS) and 0.5% N,N,N',N'-tetramethylethane-1,2-diamine (TEMED) (Thermofisher Scientific, USA) by volume. After initial cross-linking, many specimen preparation protocols call for PA to be submerged in a water-based liquid, which causes swelling by up to 21.6% to 133% in volume [38]. However, swelling is not compatible with the present specimen design, so we inhibit water diffusion into or out of the hydrogel network by submerging specimens in silicone oil. The size and shape of the specimen are preserved since the oil does not visibly swell PA and prevents the water in the hydrogel from evaporating. In this environment, PA was prone to sticking to the bottom of the dish if the oil did not form a lubricating boundary layer between the two surfaces. To ensure that the oil properly lubricates the contact surface between PA and the glass-bottom dish, we simply translated the specimen in the x_1 -direction to allow oil to pass under the PA before placing the specimen in the test device.

Hydrogel specimens for impact-rate testing with volumetric displacement measurement were molded into dogbone-shaped specimens in-place (Fig. 3C). To begin, the 3D-printed fixture was assembled in a dogbone-shaped inverse mold, creating a cavity where uncured (liquid-state) hydrogel was polymerized and permanently

adhered to the fixture. A 25 mm by 55 mm glass-bottom culture dish was treated with evaporated (tridecafluoro-1,1,2,2-tetrahydrooctyl)triethoxysilane to create a hydrophobic surface. This surface was placed on the open face of the mold, such that the hydrophobic glass treatment allowed the specimen to slide freely in the x_1 -direction, while the x_2 -direction was physically confined within the walls of the dish (Fig. 1C and 2). The specimen was then demolded and the dish was filled with the appropriate media for a specific material or cell culture. The dish was inserted into the impact device, ready for micro-tensile impact testing. When the fixture was separated using the device, the material was stretched uniaxially following a programmed motor displacement pulse.

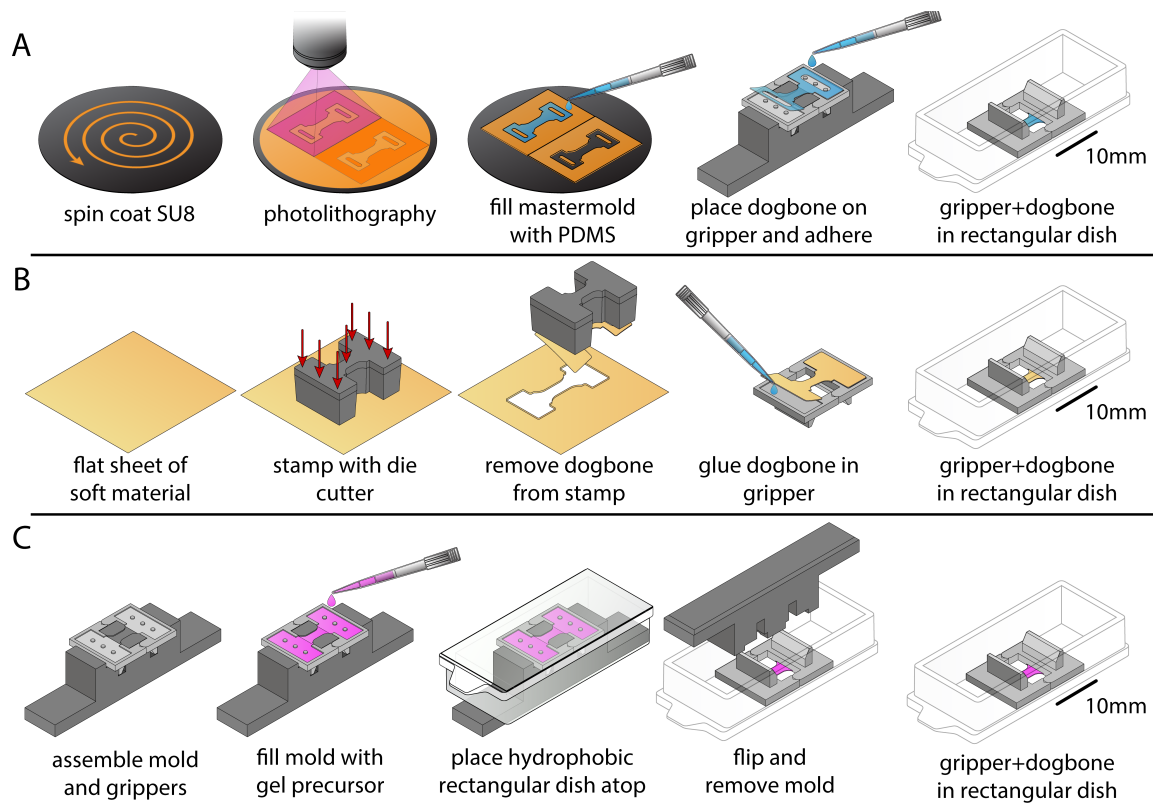


Fig. 3 Overview of specimen preparation steps for tension testing of various soft materials. (A) Dogbone specimen fabrication procedure for castable thin substrates. First, an approximately $250\ \mu\text{m}$ layer of photoresist pre-polymer (SU-8 100) was spun onto a standard 101.6 mm (4 in) silicon wafer. Then, the wafer was placed on a microscope stage and UV photocured by controlling the location of the UV light to develop a mold for a 10 mm initial length dogbone. The newly created mold was filled with a precise volume of uncured PDMS to avoid introducing a meniscus, and the specimen was cured for about 60 minutes at $60\ ^\circ\text{C}$. The PDMS dogbone was then adhered to the 3D printed specimen fixture using a thin layer of PDMS as an adhesive and cured overnight at $60\ ^\circ\text{C}$. The completed assembly could be tested immediately or sterilized and treated for *in vitro* 2D cell culture. (B) Viscoelastic soft foam materials were prepared using a die-cutting method. A sheet of soft material approximately 1 mm to 3 mm thick and a 3D printed dogbone-shaped die cutter were selected or designed based on the desired specimen geometry. Then, a uniform pressure was applied to the die cutter until it cut through the material, and the resulting dogbone was glued into the fixture and placed in a glass bottom dish for experimentation. (C) 3D tension specimen preparation procedure for castable hydrogels (i.e., Collagen-I or polyacrylamide). The specimen fixture was functionalized with a hydrophilic treatment procedure [34] and placed inside a 7 mm gauge length mold. An uncured hydrogel mixture was then poured into the compound mold created by the fixture and removable mold forming a slight meniscus. A glass bottom rectangular cell culture dish was gently placed in contact with the meniscus, flattening the contacting surface. The hydrogel was cured, the mold was removed, and the dish was flipped right-side-up and submerged in water, cell culture media, or oil depending on the application. the bottom face of the gauge section rests on the glass dish.

2.3 Programmable Device Capabilities

The PIMikroMove software included with the actuators and controllers generates a report comparing the target motor position to the measured position with a 1% standard error on the recorded data. These recorded data are exported and converted to strain, using Eqs. (1-2), to assess the capabilities of the device. Lower-rate triangular pulses tend to follow the target strain with high accuracy and precision (i.e., deviations do not exceeded the encoder noise floor). For example, in the PDMS, foam, and PA hydrogel experiments close to constant strain rates of up to approximately $15\ \text{s}^{-1}$ are demonstrated. Although possible to include in the design if needed, slack adapter configuration was avoided to allow the motioned to be reversible and non-destructive.

For *in vitro* cell culture experiments we switch to impact-like pulses (i.e., non-constant strain rate with peak rates of 100 s^{-1} or more) that test the upper limits of the actuator performance. The maximum strain rate that the motor can achieve was limited by the inertial mass internal to the actuator and the power output by the voice coil, and thus the fundamental limitation is on crosshead acceleration. Therefore, these experiment are near constant-acceleration rather than constant strain rate (see Fig. 4A). During a test, the actuator accelerates to the desired velocity within the available length limited by the desired strain on the specimen, see Fig. 4B. At this performance limit, the targeted peak strain rate is only briefly achieved at the target maximum strain amplitude. To increase the peak achievable instantaneous strain rate for each strain magnitudes, we tuned the maximum velocity, acceleration, jerk, and jounce parameters (Table 1). We also tuned the proportional–integral–derivative (PID) controller coefficients, optimizing for the most violent impact possible. Several bench-marking tests were run to assess the high-rate impact pulse generation capabilities of the device. A pulse was a success if the peak strain and peak strain rate readback from the encoder met within 1 % of the the targets programmed into the motor (Fig. 4A-B). The peak achievable strain rate for a given peak strain amplitude defines the operational limit of the device, as shown in Fig. 4C, given a nominally 7 mm initial gauge length specimen. To inform the selection of test parameters, the best-fit line to this limit is $\dot{\epsilon}_{\text{peak}} = -283.8\epsilon_{\text{peak}}e^{-0.634\epsilon_{\text{peak}}} + 319.5 \text{ s}^{-1}$. At sufficiently high strain magnitudes, we demonstrated that this device can generate peak strain rates of up to approximately 240 s^{-1} – broadly equivalent to the peak strain rates in biologically relevant blunt impacts (typically up to about 250 s^{-1}).

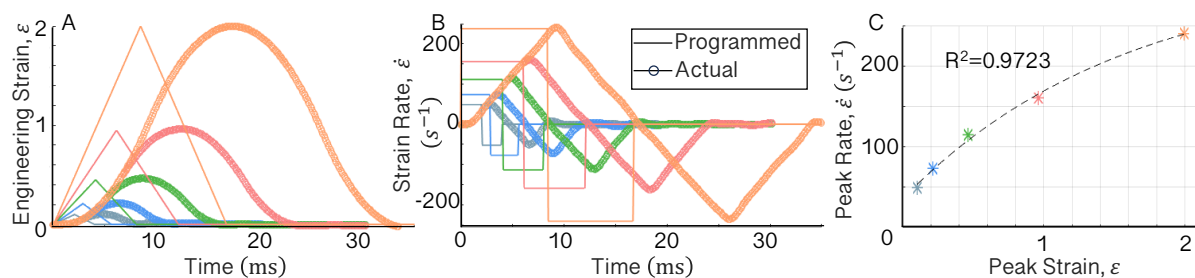


Fig. 4 The strain and strain rate capabilities plotted for an nominally 7 mm gauge length specimen. These plots must be scaled according to the strain magnitude measurements produced from studies similar to those in section 3. All results were converted to engineering strain using Eq. (1). (A) Five strain magnitudes were selected for testing the peak achievable strain rate. Here, the target triangular pulse was compared to the real motor displacement curve as measured by the real-time data recorder built into the device firmware. Uncertainties associated with the use of the V-277.631 voice coil linear actuators were estimated as 2 % linearity error and $\pm 1.0 \mu\text{m}$ bidirectional repeatability on displacement in total. (B) The derivative of the strain profile was plotted to show that the peak acceleration was reached long before the peak velocity, demonstrating that acceleration is the main limiting factor of the device. Note that the target peak strain rate is reached only briefly before turnaround, indicating this is a upper limit of the device performance envelope. (C) Peak strain rate plotted against the peak strain amplitude to define a performance curve for the device.

3 Results

To validate the device in 2D and 3D, images were acquired during both quasi-static strain rate (10^{-6} s^{-1}) and intermediate strain rate (10^0 s^{-1} to 10^2 s^{-1}) tension experiments. These images were taken while the device was mounted to an inverted microscope (Nikon Ti-2; Melville, NY), connected to multi-photon microscopy (Coherent - Chameleon, Santa Clara, CA), custom-built light field microscopy [39], and epifluorescence microscopy systems. The frame rate and quantum efficiency of these systems were the limiting factors when acquiring image data at high speeds (> 100 frames per second). Experimental strain rates in the range of 10^{-6} s^{-1} to 10^1 s^{-1} were selected to balance acquisition speed with signal-to-noise quality in the attained images.

3.1 Homogeneous 2D-DIC Strain in PDMS

The strain field experienced by the nominally 2D PDMS specimens (Fig. 3A) were evaluated by tracking the applied deformations from the tension device using Augmented Lagrangian Digital Image Correlation (ALDIC) [40]². The bottom (imaged) surface of the specimen was prepared by applying black acrylic ink (Liquitex Artist Materials, Piscataway, NJ) with an airbrush (HP-C Plus; Iwata Medea Inc, Portland, OR) to create a random speckle pattern (Fig. 5 A). Images were acquired with a high speed camera (Photometrics, Kinetix sCMOS, Tuscon, AZ) using the bright field setup on the microscope described above and a 2X magnification objective during the applied

² See: <https://www.mathworks.com/matlabcentral/fileexchange/70499-augmented-lagrangian-digital-image-correlation-and-tracking>

deformations. The experimental parameters are further detailed in Table 2. As the stretched portion of the specimen was not constrained to strictly in-plane motion, loss of focus as the specimen was stretched due to the Poisson effect or minor misalignment was avoided by choosing the aforementioned 2X microscope objective, which has a comparatively large depth of field. Using optics theory, the approximate depth of field is between $138\ \mu\text{m}$ and $250\ \mu\text{m}$ [41] compared to out-of-plane motion of approximately $25\ \mu\text{m}$ in a typical experiment. Hence this out-of-plane motion is comparatively small in the x_3 -direction, and therefore the parasitic strain (i.e., out-of-plane bias error) is minimal compared to the large specimen deformations.

All images were processed with the ALDIC method to measure the full-field deformations in the gauge region of the specimen. ALDIC combines local subset DIC and finite element-based DIC for more robust and accurate tracking of deformed images. One of the main advantages of the ALDIC method over other DIC packages is that its correlation cost function simultaneously solves for the displacement and displacement gradient field, which then makes extraction of the material strain fields and other material properties straightforward [40]. Here, from the deformation gradient output the mean Poisson's ratio of the material was calculated to be 0.464 ± 0.097 , comparable to literature values between 0.45 and 0.5 for PDMS made with Sylgard 184 [42–45]. In another study, Cho et al. reported 0.4999 ± 0.0011 [42]. Examining the spatial character of the reconstructed displacement field (Fig. 5B) in more detail, we find a relatively homogeneous displacement and constant strain field across the image field of view, as expected. Furthermore, the calculated mean and standard deviation of Lagrange strains (Fig. 5C) showed nearly linear deformation and no shear. There was a slight deviation near the peak due to the inertial effects in the system during reversal, but these experiments demonstrated the ability of the device to apply a uniform strain field to our 2D substrates at intermediate strain rates.

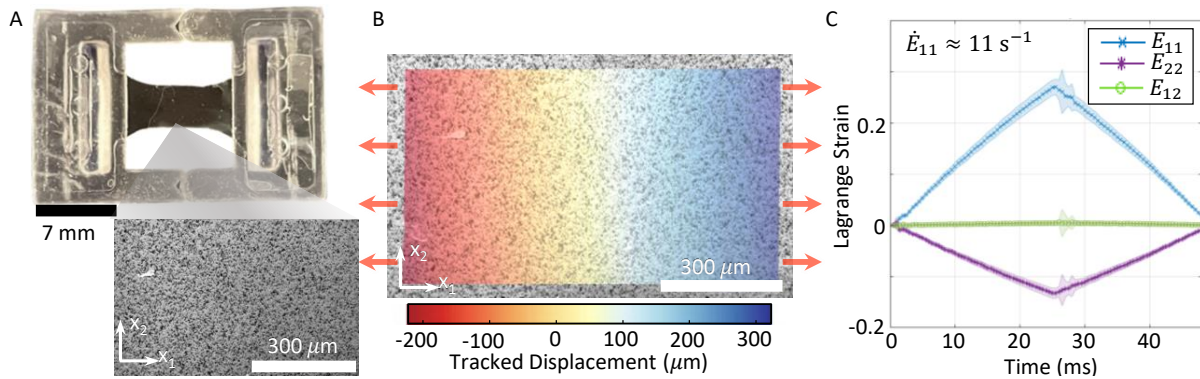


Fig. 5 Intermediate strain rate ($\approx 11\ \text{s}^{-1}$) displacement and strain field assessment of a PDMS dogbone specimen under simple tension. (A) Photo of a PDMS dogbone prepared with a random speckle patterned surface in the gauge region. *Inset*: Example field of view of the speckle pattern used for the displacement and strain measurement. (B) The x_1 -displacement field at maximum deformation, tracked with ALDIC [40] and overlaid onto the specimen surface. The uniformly linear variation centered close to zero displacement demonstrates that the stationary point of the deformation is captured. (C) Measured Lagrange strain, mean (solid line) ± 1 standard deviation (shaded area) in the field of view, shows acceptable linearity and limited scatter as a function of test time relative to testing requirements.

3.2 Heterogeneous 2D-DIC Strain in Polyurethane Foam

To demonstrate the universality of the device on a more microstructurally complex material, we subjected an open-cell polyurethane-based foam (Poron XRD 095, Rogers Corp, Rogers, CT), to a dynamic strain rate of $\approx 15\ \text{s}^{-1}$, whose quasi-static continuum-scale mechanical properties were characterized in Landauer, et al. [46] and linear viscoelastic properties were reported in [47]. Briefly, dogbone-shaped foam specimens were cut from foam sheets using a customized die cutter as described in section 2.2.2. Next, the foam surface was airbrushed with a black background coat of acrylic ink (Liquitex Artist Materials, Piscataway, NJ) followed by a white speckle layer (Golden Artist Colors Inc., New Berlin, NY). All specimen deformations were imaged using the same bright field microscopy system and settings as described above, and analyzed using the ALDIC algorithm [40] (Fig. 6B). The spatially-averaged, axial Lagrange strain was extracted using the methods described in Landauer et. al. [46], and is plotted in Fig. 6C as a function of time. While the ALDIC accurately resolves a locally heterogeneous strain field for this particular foam specimen, the average strain follows the applied strain closely during the loading portion. Slight, yet noticeable, creep is visible during the unloading portion of the applied strain pulse when the "fingers" disengage from the fixture. Overall, both the PDMS and foam test cases show that the device is well-suited for applying uniaxial stress to each specimen at intermediate loading strain rates between $\approx 11\ \text{s}^{-1}$ and $\approx 15\ \text{s}^{-1}$.

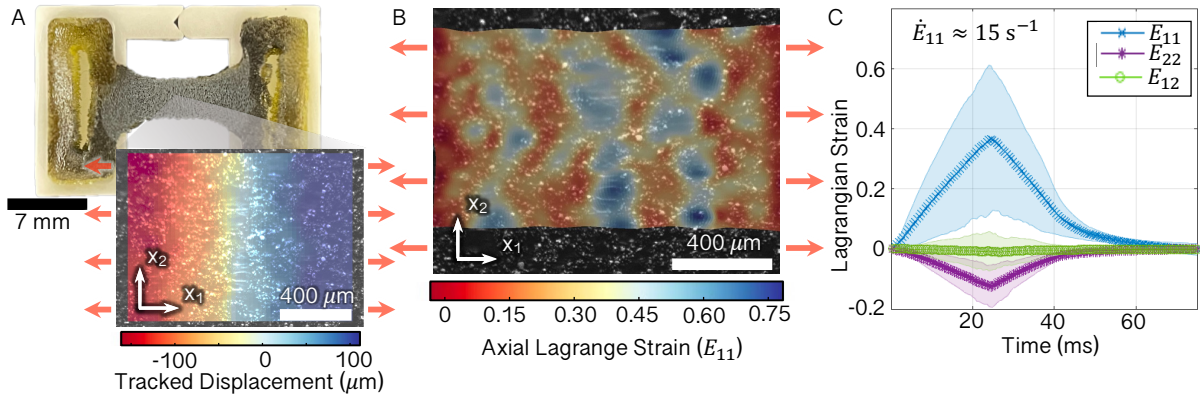


Fig. 6 Intermediate strain rate ($\approx 15 \text{ s}^{-1}$) displacement and strain field measurement of a simple tension experiment on a viscoelastic open-cell foam dogbone analyzed using ALDIC. (A) An example photo of a foam specimen prepared with a random speckle patterned surface. *Inset*: A typical axial (u_1) displacement field overlayed on the speckled specimen surface in the field of view. (B) The axial Lagrange strain field mapped on the specimen's surface at maximum deformation, showing strain localization and banding in the foam specimen. (C) Mean (solid line) and one standard deviation (shaded area) of the mean axial, lateral, and shear Lagrange strains in the DIC field of view versus time, showing overall linearity with time, following the prescribed motion. Comparing the mean strain field values with those of Fig. 5, the dramatic increase in standard deviation due to localization is clearly visible. A small amount of expected specimen creep is visible during the unloading portion of the strain versus time curve.

3.3 Volumetric 3D Strain in PA Hydrogel

To assess the spatiotemporal character of the device-generated volumetric strain fields, we deploy a two-pronged approach. First, we assess the uniformity of the *in-situ* strain field by employing high-resolution, multiphoton microscopy imaging at quasi-static strain rates. This technique has been shown to provide excellent spatial information, but is limited in its ability to provide temporal data due to the intrinsic scanning-based image acquisition time. Thus, to overcome this temporal hurdle, we employ our recently developed High Rate-Volumetric Particle Tracking Microscopy (HR-VPTM) technique [39] to resolve the volumetric 3D strain fields at elevated rates but with reduced spatial resolution.

3.3.1 Quasi-static Volumetric 3D Strain via Digital Volume Correlation

For the high-resolution, low-rate quasistatic validation of the device, we embedded 1 μm -diameter fluorescent polystyrene particles into polyacrylamide (PA) hydrogel specimens (Fig. 7A) by mixing a small volume ratio of particles in solution into the gel prior to crosslinking. Using multi-photon microscopy [48] with a 20X microscope objective, a series of high-resolution volumetric images was acquired during the step-wise deformation of the specimen. After each load step, a volumetric image stack was captured following a 30 sec hold to mitigate viscous, inertial, and other time-dependent effects. Using these high-resolution, densely seeded particle image volumes, we quantitatively tracked the full-field displacement and strain fields to assess the spatial nature and uniformity of the applied deformation field.

Here, three-dimensional step-wise displacements and strain fields were reconstructed using our Augmented Lagrangian Digital Volume Correlation (ALDVC) open-source code package [49]³. Each volumetric image stack is in the same size of 2048 voxels by 512 voxels by 281 voxels. The unit conversion ratio for our dataset is [0.2, 0.2, 1.075] $\mu\text{m}/\text{voxel}$. We chose each DVC local subset size as 64 voxels by 64 voxels by 32 voxels with 50% overlapping with its neighboring subset. The step size of DVC local subset centroids is 32 voxels by 32 voxels by 16 voxels. We considered the ICGN and ADMM iterations to converge when the L_2 norm of the displacement update vector was less than 0.01 voxels. To track large finite deformations where the maximum uniaxial strain was about 30%, incremental tracking mode was used in ALDVC. In incremental tracking, each volumetric image stack is compared to the subsequent volumetric image stack. All tracked incremental displacement segments from each image pair were then merged and interpolated to compute the overall cumulative displacements (total net displacements compared to the first, undeformed image stack) at each time step. To compute the local strain tensor, a variety of user-chosen finite-difference operators [3] can be applied with the simplest one consisting of a local, least-squared plane fitting approach using a kernel (or stencil) size of $3 \times 3 \times 3$ neighboring data points (see Fig. 7C). From these strains, the Poisson's ratio for the PA specimen was calculated as 0.494 ± 0.082 .

³ See: <https://github.com/FranckLab/ALDVC>

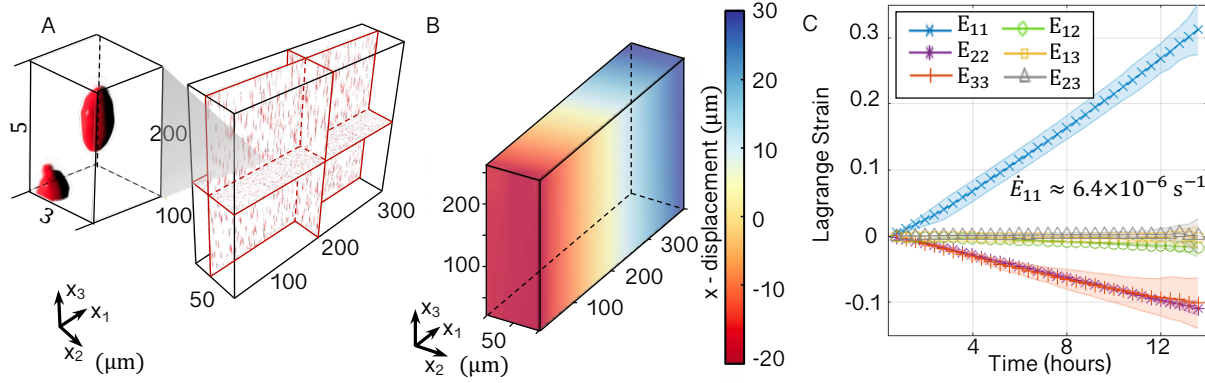


Fig. 7 Quasi-static, high spatial resolution volumetric displacement and strain field validation conducted using Augmented Lagrangian Digital Volume Correlation (ALDVC) [49]. (A) A slice view of a representative, volumetrically reconstructed multi-photon image of $1\ \mu\text{m}$ fluorescent particles embedded in a polyacrylamide (PA) hydrogel specimen. *Inset*: A magnified, view of a single $1\ \mu\text{m}$ particle within the 3D volume. (B) ALDVC computed x_1 -displacement field of a representative volume illustrating that the specimen is experiencing uniform deformation with a stationary point in the DVC field of view. (C) Spatially-averaged 3D Lagrange strain components as a function of total test time, shown as above with mean (solid line) ± 1 standard deviation (shaded area).

3.3.2 Intermediate strain-rate, Volumetric 3D Strain via High Rate-Volumetric Particle Tracking Microscopy

To validate, or assess, the volumetric strain fields at significantly higher strain rates, e.g., on the order of $1\ \text{s}^{-1}$ to $100\ \text{s}^{-1}$ we utilized our previously developed High Rate-Volumetric Particle Tracking Microscopy (HR-VPTM) technique [39]⁴. The advantage of this technique is that 3D volumetric data can be reconstructed from temporally highly resolved 2D images using the principle of light field microscopy. Here, we measured the 3D volumetric deformation of the tensile specimen as it undergoes an impact up to $7\ \text{s}^{-1}$ at 200 frames per second (fps). This data was used to assess the strain fields as a function of space and time during the impact event. We embedded a layer of $10\ \mu\text{m}$ diameter fluorescent microparticles into a polyacrylamide hydrogel dogbone specimen. The size and spacing of particles is directly related to the recoverable spatial resolution. From this perspective, smaller particles would be preferred, however, due to the higher loading rates, and thus shorter camera shutter times, the overall photon count and thus signal-to-noise (SNR) in the acquired images is lower than in the quasi-static case. To provide the highest spatial resolution capture with a SNR amenable to complete volumetric 3D reconstruction of the imaged space we chose $10\ \mu\text{m}$ diameter fluorescent microparticles. More details on the trade-off between particle size and 3D image reconstruction quality can be found elsewhere [39]. In our device, the emitted light was collected by a $4\times/0.20$ numerical aperture (NA) objective, passed through a microlens array, and collected by a high-speed camera (Phantom v2511, Vision Research, Wayne, NJ) with a $4\times$ transfer objective (Fig. 8A). The camera was triggered at the same time as the voice coil linear actuators, and a high-rate video of the deformation was collected. This 2D image series was then deconvolved into a series of 3D fluorescent particle images (Fig. 8B), and analyzed using the HR-VPTM method [39] (Table 3). The tracked particle trajectories are plotted using visualization scripts from SerialTrack [50] in Fig. 8C & E. The strains plotted in Fig. 8D & F were used to calculate the Poisson's ratio as 0.391 ± 0.028 and 0.414 ± 0.019 , respectively. The mean values from both experiments were within 5.6% of each other. The particle motion was found to be consistent with the uniaxial tension of a homogeneous, isotropic, linear elastic material. It should be noted that due to slight misalignment of the specimen within the device, HR-VPTM had difficulties localizing the center of some of the particles along the x_3 -direction (Fig. 8C). This leads to more noisy displacement and strain estimate in the resulting x_3 -based data (i.e., E_{13} , E_{23} , E_{33}) than in the in-plane components. Nevertheless, these 3D measurements demonstrate the capability of the device to produce a well-characterized simple tension state at intermediate strain rates ($0.7\ \text{s}^{-1}$ to $7\ \text{s}^{-1}$).

3.4 Impact-like Deformation of 2D and 3D Cell Culture Systems

One of the intrinsic advantages of the design of this device is the ability to deform specimens under hydrated and/or sterile conditions. This facilitates the use of the design with biological specimens from *in vitro* cell cultures to tissue specimens. To demonstrate this capability in a specific application, we subject both 2D and 3D *in vitro* neural cell cultures to prescribed simple tension, single pulse impacts. For sterility, the 3D printed fixture, dogbone molds, and PDMS substrates were autoclaved and handled in a biosafety cabinet. To prepare 2D neural cell cultures, specimens fabricated according to the procedure laid out in section 2.2.1 were autoclaved for one hour. Primary cortical neural

⁴ See: <https://github.com/FranckLab/HR-VPTM>

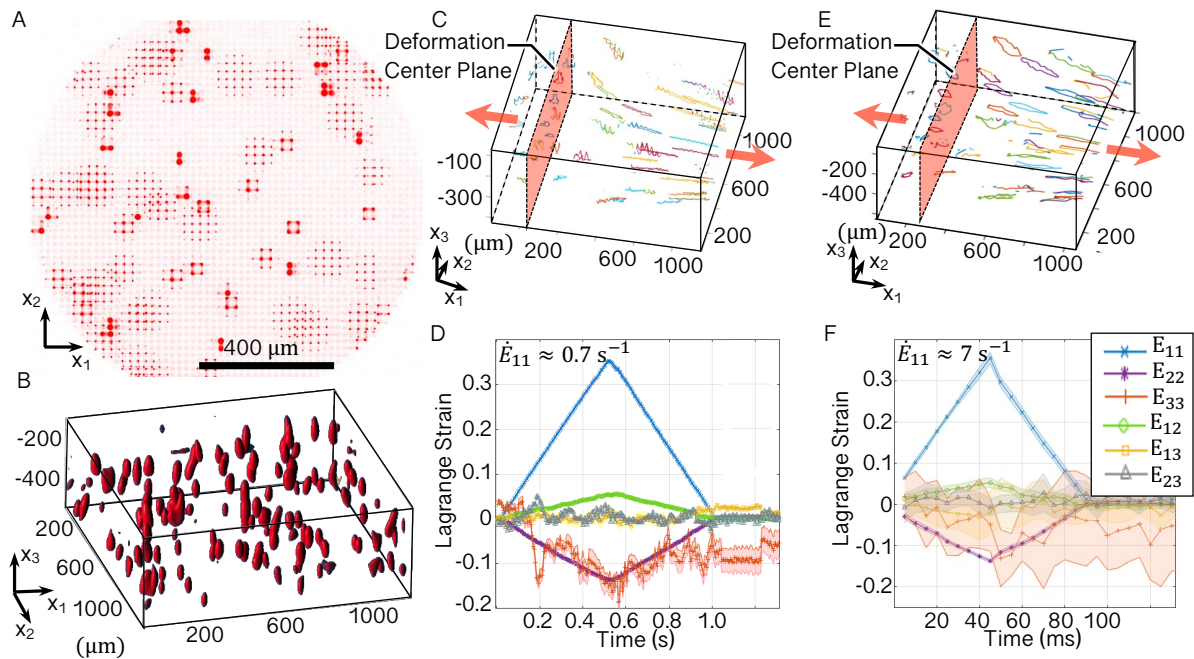


Fig. 8 High-speed volumetric strain field validation using HR-VPTM [39]. (A) Example false color image of 10 μm fluorescent particles embedded in a PA dogbone tensile specimen and imaged through a microlens array at 200 frames per second. (B) Volume view of the 3D reconstruction of the 10 μm particles. (C) Deformations at 0.7 s^{-1} were recorded and reconstructed particle trajectories are shown using the particle trace visualization tool built into HR-VPTM. The traces show uniform deformations, centered approximately about the red plane inserted at the estimated stationary plane of the symmetric deformation. Traces are as expected from a uniaxial stress field in the x_1 - and x_2 -directions, with slightly higher variability in the x_3 -direction. (D) The resultant mean ± 1 standard deviation strain field as a function of time, showing the expected axial behaviors and comparatively small shear components. (E) A higher rate experiment at approximately 7 s^{-1} , showing similar traces indicating uniaxial tension-dominated deformation. (F) Mean ± 1 standard deviation and over the reconstruction field of view, showing that the strain maintained uniformity at elevated strain rates. Variability in the x_3 -direction traces is also notable in the computed E_{33} and E_{23} Lagrange strain results as a larger standard deviation from the mean.

cells were harvested from postnatal day (P) 0-1 Sprague-Dawley rats, following the protocol established in Scimone et al. [34]. The center of the PDMS dogbone is treated with 40 μL of poly-D-lysine and laminin (4 $\mu\text{g}/\text{mL}$) solution for one hour to functionalize the surface for cell attachment. The laminin solution was then washed three times with 1 \times Phosphate Buffered Saline (PBS), and a solution containing 700 000 cells/mL of the neural cell is deposited in the center of the dogbone and cultured for up to 21 days. Cells were then stained for 15 minutes with a live-cell indicator cell-permanent dye (Invitrogen Calcein-AM). To apply the device to a 3D cell culture system, neural cells were embedded in 3D collagen-I hydrogels by combining the protocols laid out in Scimone et. al. [34] with the specimen preparation procedure in figure 3C. Primary cortical cells were seeded at a concentration of 12.3 million cells/mL, and molded into a dogbone specimen with a 2 mm thickness. Cells were matured in an incubator for 7 days to allow for complete synaptogenesis and subsequently stained for 45 minutes with Calcein-AM. Both of these culture models were then stretched using our impact device and imaged in their undeformed and deformed states (Fig. 9) using multi-photon microscopy.

4 Conclusion

Quantitative, physical characterization of complex soft and biological materials often requires full spatiotemporal access during the deformation process. Furthermore, as many materials belonging to the soft matter class exhibit pronounced viscoelasticity, being able to control and measure strain rates over several decades in magnitude becomes an important design trait. This is particularly important when studying the failure or injury response for biological systems in the intermediate (impact) strain rate regime (1 s^{-1} to 100 s^{-1}). In this paper, we address this need by presenting a highly versatile micro-tensile impact device for soft materials and *in vitro* cellular injury and biomechanics investigations. The device was particularly designed to be capable of generating a large envelope of engineering strains ($O(1)\%$ to $O(200)\%$) and strain rates (about 10^{-6} s^{-1} to a peak rate of approximately 240 s^{-1}). The open-source, adaptable nature of this device provides significant user flexibility and compatibility for integration with other existing experimental platforms and measurement capabilities, including high-resolution force sensing, 2D cell patterning on flexible membranes, electrical activity monitoring of neural cells following an injury, high-rate stretch of large tissue slices, and repetitive loading of soft materials in 2D and 3D configurations.

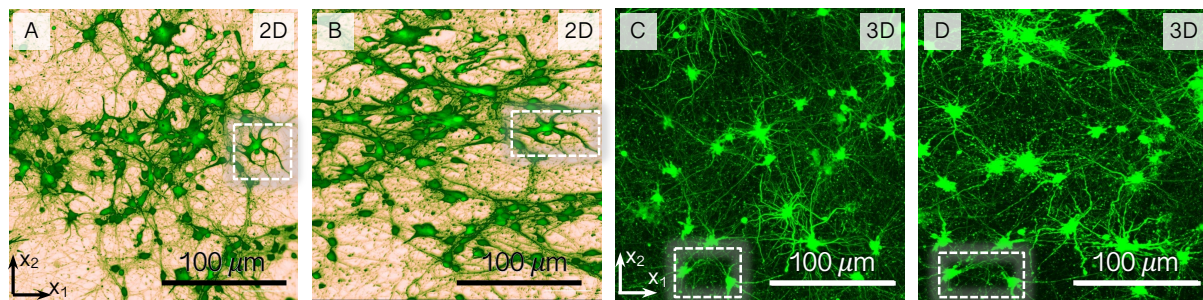


Fig. 9 Simple tension deformations applied to the 2D neural cell culture substrate with surface-attached cells or the and 3D culture system with its embedded neural cells. Cell cultures were live stained with Calcein-AM, stretched, and imaged at peak deformation. (A) A representative epi-fluorescent micrograph with a customized lookup table of Calcein-AM stained primary neural cells grown on 2D PDMS substrates prior to applied deformation. (B) Representative epi-fluorescent micrograph of the same cell culture as in (A) having been deformed to ca. 53 % crosshead engineering strain in the x_1 -direction. The white box showcases individual cells that were stretched consistent with the deformation fields presented in Fig. 5. (C) Representative, undeformed configuration maximum intensity projection of a (200 μm thick) volumetric multiphoton image stack of neural cells grown in a 3D collagen-I hydrogel. (D) Representative, deformed configuration (ca. 28 % crosshead engineering strain) maximum intensity projection of a volumetric multiphoton image stack in the same region as shown in (C), again with a box added to highlight the change in two cells in the field of view. A multi-cell cluster is brought into the field of view (upper left) post-deformation due to the Poisson's effect contraction of the material in the x_2 direction.

Acknowledgements This material is based upon research supported by the U. S. Office of Naval Research under PANTHER award number N000142112044 through Dr. Timothy Bentley.

Data availability

Datasets used in the preparation of this paper - design and validation - are available on the MINDS@UW server (<http://digital.library.wisc.edu/1793/83802>). Parts, control scripts, and functions used to analyze the data and to produce results shown in the figures above are available at <https://github.com/FranckLab/Intermediate-Rate-Tension-Device>.

Author contributions

C.F., J.Z., and L.S. conceived of the design requirements that the device must achieve. L.S. designed, prototyped, fabricated, and validated the electro-mechanical aspects of the impact device. A.D., J.Z., and L.S. developed the 3D specimen fabrication and collagen-I hydrogel neural cell culture protocols. J.S., J.P., J.Z., A.M., and L.S. developed the 2D PDMS specimen fabrication and 2D neural cell culture protocols. L.S. conducted the high-rate and low-rate 3D strain field validation experiments. Data were processed by A.L, J.Y, and L.S.. 2D strain field validation on PDMS and polyurethane foam experiments and data analysis were conducted by J.S., J.T., and L.S.. L.S., A.L., and C.F. wrote the manuscript with contributions from J.S., A.D., J.Y., and J.Z.. C.F., A.L., J.Z., and L.S. oversaw the experiments and analyses. All authors reviewed and approved the manuscript.

Conflict of interest

The authors declare that they have no conflict of interest. Certain commercial equipment, software and/or materials are identified in this paper in order to adequately specify the experimental procedure. In no case does such identification imply recommendation or endorsement by the National Institute of Standards and Technology, nor does it imply that the equipment and/or materials used are necessarily the best available for the purpose.

References

1. Koumlis, S. & Lamberson, L. Strain Rate Dependent Compressive Response of Open Cell Polyurethane Foam. *Experimental Mechanics* **59**, 1087–1103 (2019). URL <http://link.springer.com/10.1007/s11340-019-00521-3>.
2. Lakes, R. S. *Viscoelastic Solids* (1998) (CRC Press, 2017). Google-Books-ID: sEkPEAAAQBAJ.
3. Bar-Kochba, E., Toyjanova, J., Andrews, E., Kim, K.-S. & Franck, C. A Fast Iterative Digital Volume Correlation Algorithm for Large Deformations. *Experimental Mechanics* **55**, 261–274 (2015). URL <http://link.springer.com/10.1007/s11340-014-9874-2>.
4. Hyun, K. et al. A review of nonlinear oscillatory shear tests: Analysis and application of large amplitude oscillatory shear (LAOS). *Progress in Polymer Science* **36**, 1697–1753 (2011). URL <https://linkinghub.elsevier.com/retrieve/pii/S0079670011000281>.

5. Distler, T., Schaller, E., Steinmann, P., Boccaccini, A. & Budday, S. Alginate-based hydrogels show the same complex mechanical behavior as brain tissue. *Journal of the Mechanical Behavior of Biomedical Materials* **111**, 103979 (2020). URL <https://linkinghub.elsevier.com/retrieve/pii/S1751616120305312>.
6. Monnerie, H. *et al.* Dendritic alterations after dynamic axonal stretch injury in vitro. *Experimental Neurology* **224**, 415–423 (2010). URL <https://linkinghub.elsevier.com/retrieve/pii/S0014488610001597>.
7. Franck, C., Hong, S., Maskarinec, S. A., Tirrell, D. A. & Ravichandran, G. Three-dimensional Full-field Measurements of Large Deformations in Soft Materials Using Confocal Microscopy and Digital Volume Correlation. *Experimental Mechanics* **47**, 427–438 (2007). URL <https://link.springer.com/10.1007/s11340-007-9037-9>.
8. Hazlett, L. *et al.* Epifluorescence-based three-dimensional traction force microscopy. *Scientific Reports* **10**, 16599 (2020). URL <https://www.nature.com/articles/s41598-020-72931-6>.
9. Braun, N. J., Liao, D. & Alford, P. W. Orientation of neurites influences severity of mechanically induced tau pathology. *Biophysical Journal* **120**, 3272–3282 (2021). URL <https://linkinghub.elsevier.com/retrieve/pii/S0006349521005956>.
10. Estrada, J. B., Cramer, H. C., Scimone, M. T., Buyukozturk, S. & Franck, C. Neural cell injury pathology due to high-rate mechanical loading. *Brain Multiphysics* **2**, 100034 (2021). URL <https://www.sciencedirect.com/science/article/pii/S2666522021000149>.
11. Carlsen, R. W., Fawzi, A. L., Wan, Y., Kesari, H. & Franck, C. A quantitative relationship between rotational head kinematics and brain tissue strain from a 2-D parametric finite element analysis. *Brain Multiphysics* **2**, 100024 (2021). URL <https://linkinghub.elsevier.com/retrieve/pii/S2666522021000046>.
12. Chen, W. W. & Song, B. Kolsky Compression Bar Experiments at Intermediate Strain Rates. In *Split Hopkinson (Kolsky) Bar*, 291–311 (Springer US, Boston, MA, 2011). URL http://link.springer.com/10.1007/978-1-4419-7982-7_9. Series Title: Mechanical Engineering Series.
13. Cullen, D. K. & LaPlaca, M. C. Neuronal Response to High Rate Shear Deformation Depends on Heterogeneity of the Local Strain Field. *Journal of Neurotrauma* **23**, 1304–1319 (2006). URL <http://www.liebertpub.com/doi/10.1089/neu.2006.23.1304>.
14. Elhebeary, M., Emon, M. A. B., Aydin, O. & Saif, M. T. A. A novel technique for in situ uniaxial tests of self-assembled soft biomaterials. *Lab on a chip* **19**, 1153–1161 (2019).
15. Zhang, S., Galuska, L. A. & Gu, X. Water-assisted mechanical testing of polymeric thin-films. *Journal of Polymer Science* **60**, 1108–1129 (2022). URL <https://onlinelibrary.wiley.com/doi/abs/10.1002/pol.20210281>.
16. Subramanian, G., Elsaadany, M., Bialorucki, C. & Yildirim-Ayan, E. Creating Homogenous Strain Distribution within 3D Cell-encapsulated Constructs Using a Simple and Cost-effective Uniaxial Tensile Bioreactor: Design and Validation Study. *Biotechnology and bioengineering* **114** (2017).
17. Massai, D. *et al.* Bioreactor Platform for Biomimetic Culture and in situ Monitoring of the Mechanical Response of in vitro Engineered Models of Cardiac Tissue. *Frontiers in Bioengineering and Biotechnology* **8**, 733 (2020). URL <https://www.frontiersin.org/article/10.3389/fbioe.2020.00733>.
18. Janvier, A. J., Canty-Laird, E. & Henstock, J. R. A universal multi-platform 3D printed bioreactor chamber for tendon tissue engineering. *Journal of Tissue Engineering* **11**, 2041731420942462 (2020). URL <https://doi.org/10.1177/2041731420942462>.
19. Schwan, J. *et al.* Anisotropic engineered heart tissue made from laser-cut decellularized myocardium. *Scientific Reports* **6**, 32068 (2016). URL <https://www.nature.com/articles/srep32068>.
20. Win, Z. *et al.* Cellular Microbiaxial Stretching to Measure a Single-Cell Strain Energy Density Function. *Journal of Biomechanical Engineering* **139**, 071006 (2017). URL <https://asmedigitalcollection.asme.org/biomechanical/article/doi/10.1115/1.4036440/371391/Cellular-Microbiaxial-Stretching-to-Measure-a>.
21. Terpsma, R. & Hovey, C. Blunt Impact Brain Injury using Cellular Injury Criterion. Tech. Rep. SAND–2020-11444, 1716577, 692091, Sandia National Lab (2020). URL <https://www.osti.gov/biblio/1716577>.
22. Zou, H., Schmiedeler, J. P. & Hardy, W. N. Separating brain motion into rigid body displacement and deformation under low-severity impacts. *Journal of Biomechanics* **40**, 1183–1191 (2007). URL <https://linkinghub.elsevier.com/retrieve/pii/S0021929006002314>.
23. Sabet, A. A., Christoforou, E., Zatin, B., Genin, G. M. & Bayly, P. V. Deformation of the human brain induced by mild angular head acceleration. *Journal of Biomechanics* **41**, 307–315 (2008). URL <https://linkinghub.elsevier.com/retrieve/pii/S0021929007003880>.
24. Budday, S. *et al.* Mechanical properties of gray and white matter brain tissue by indentation. *Journal of the Mechanical Behavior of Biomedical Materials* **46**, 318–330 (2015). URL <https://www.sciencedirect.com/science/article/pii/S1751616115000673>.
25. Li, X., Tao, J., Landauer, A. K., Franck, C. & Henann, D. L. Large-deformation constitutive modeling of viscoelastic foams: Application to a closed-cell foam material. *Journal of the Mechanics and Physics of Solids* **161**, 104807 (2022). URL <https://www.sciencedirect.com/science/article/pii/S0022509622000254>.
26. Jiang, M. *et al.* Clamping soft biologic tissues for uniaxial tensile testing: A brief survey of current methods and development of a novel clamping mechanism. *Journal of the Mechanical Behavior of Biomedical Materials* **103**, 103503 (2020). URL <https://linkinghub.elsevier.com/retrieve/pii/S1751616119310628>.
27. Jacquemoud, C., Bruyere-Garnier, K. & Coret, M. Methodology to determine failure characteristics of planar soft tissues using a dynamic tensile test. *Journal of Biomechanics* **40**, 468–475 (2007). URL <https://linkinghub.elsevier.com/retrieve/pii/S0021929005005543>.
28. Rosas-Hernandez, H. *et al.* Characterization of uniaxial high-speed stretch as an in vitro model of mild traumatic brain injury on the blood-brain barrier. *Neuroscience Letters* **672**, 123–129 (2018). URL <https://linkinghub.elsevier.com/retrieve/pii/S0304394018300958>.
29. Cui, J., Shi, Y., Zhang, X., Huang, W. & Ma, M. Experimental study on the tension and puncture behavior of spray polyurea at high strain rates. *Polymer Testing* **93**, 106863 (2021). URL <https://www.sciencedirect.com/science/article/pii/S0142941820320924>.
30. Fast-Irvine, C., Abedini, A., Noder, J. & Butcher, C. An Experimental Methodology to Characterize the Plasticity of Sheet Metals from Uniaxial to Plane Strain Tension. *Experimental Mechanics* **61**, 1381–1404 (2021). URL <https://doi.org/10.1007/s11340-021-00744-3>.
31. Rahmat, M., Backman, D. & Desnoyers, R. Intermediate Strain Rate Material Characterization with Digital Image Correlation. *JoVE* e59168 (2019). URL <https://www.jove.com/59168>.
32. Pfister, B. J., Weihs, T. P., Betenbaugh, M. & Bao, G. An In Vitro Uniaxial Stretch Model for Axonal Injury. *Annals of Biomedical Engineering* **31**, 589–598 (2003). URL <http://link.springer.com/10.1114/1.1566445>.
33. Scholze, M. *et al.* Standardized tensile testing of soft tissue using a 3D printed clamping system. *HardwareX* **8**, e00159 (2020). URL <https://linkinghub.elsevier.com/retrieve/pii/S2468067220300687>.
34. Scimone, M. T. *et al.* Modular approach for resolving and mapping complex neural and other cellular structures and their associated deformation fields in three dimensions. *Nature Protocols* **13**, 3042–3064 (2018). URL <http://www.nature.com/articles/s41596-018-0077-7>.

35. Estrada, J., Barajas, C., Henann, D., Johnsen, E. & Franck, C. High strain-rate soft material characterization via inertial cavitation. *Journal of the Mechanics and Physics of Solids* **112**, 291–317 (2018). URL <https://doi.org/10.1016/j.jmps.2017.12.006>.
36. López-Fagundo, C., Bar-Kochba, E., Livi, L. L., Hoffman-Kim, D. & Franck, C. Three-dimensional traction forces of Schwann cells on compliant substrates. *Journal of The Royal Society Interface* **11**, 20140247 (2014). URL <https://royalsocietypublishing.org/doi/10.1098/rsif.2014.0247>.
37. Boudou, T., Ohayon, J., Picart, C. & Tracqui, P. An extended relationship for the characterization of Young's modulus and Poisson's ratio of tunable polyacrylamide gels. *Biorheology* **43**, 721–728 (2006). URL <https://content.iospress.com/articles/biorheology/bir442>. Publisher: IOS Press.
38. Subramani, R. et al. The Influence of Swelling on Elastic Properties of Polyacrylamide Hydrogels. *Frontiers in Materials* **7**, 212 (2020). URL <https://www.frontiersin.org/article/10.3389/fmats.2020.00212/full>.
39. Buyukozturk, S. et al. High-Speed, 3D Volumetric Displacement and Strain Mapping in Soft Materials Using Light Field Microscopy. *Experimental Mechanics* (2022). URL <https://link.springer.com/10.1007/s11340-022-00885-z>.
40. Yang, J. & Bhattacharya, K. Augmented Lagrangian Digital Image Correlation. *Experimental Mechanics* **59**, 187–205 (2019). URL <http://link.springer.com/10.1007/s11340-018-00457-0>.
41. Spring, K. & Davidson, M. Depth of Field and Depth of Focus. URL <https://www.microscopyu.com/microscopy-basics/depth-of-field-and-depth-of-focus>.
42. Cho, H. S., Kim, H. A., Seo, D. W. & Jeoung, S. C. Poisson's ratio measurement through engraving the grid pattern inside poly(dimethylsiloxane) by ultrafast laser. *Japanese Journal of Applied Physics* **60**, 101004 (2021). URL <https://iopscience.iop.org/article/10.35848/1347-4065/ac2424/meta>.
43. Park, J. S., Cabosky, R. & Zhijiang Ye, I. I. K. Investigating the mechanical and optical properties of thin pdms film by flat-punched indentation. *Optical Materials* **85**, 153–161 (2018). URL <https://www.sciencedirect.com/science/article/pii/S0925346718305895#fig5>.
44. Pritchard, R. H., Lava, P., Debruyne, D. & Terentjev, E. M. Precise determination of the poisson ratio in soft materials with 2d digital image correlation. *Soft Matter* **9**, 6037–6045 (2013). URL <https://pubs.rsc.org/en/content/articlelanding/2013/sm/c3sm50901j>.
45. Muller, A., Wapler, M. C. & Wallrabe, U. A quick and accurate method to determine the poisson's ratio and the coefficient of thermal expansion of pdms. *Soft Matter* **15**, 779–784 (2018). URL <https://pubs.rsc.org/en/content/articlelanding/2019/sm/c8sm02105h>.
46. Landauer, A. K., Li, X., Franck, C. & Henann, D. L. Experimental characterization and hyperelastic constitutive modeling of open-cell elastomeric foams. *Journal of the Mechanics and Physics of Solids* **133**, 103701 (2019). URL <https://www.sciencedirect.com/science/article/pii/S0022509619303825>.
47. Landauer, A. K., Kafka, O. L., Moser, N. H. & Forster, A. M. A materials dataset for elastomeric foam impact mitigating materials (2022). URL https://petreldata.net/mdf/detail/foam_db_v1.1.
48. Hoover, E. E. & Squier, J. A. Advances in multiphoton microscopy technology. *Nature Photonics* **7**, 93–101 (2013). URL <http://www.nature.com/articles/nphoton.2012.361>.
49. Yang, J., Hazlett, L., Landauer, A. & Franck, C. Augmented Lagrangian Digital Volume Correlation (ALDVC). *Experimental Mechanics* **60**, 1205–1223 (2020). URL <https://link.springer.com/10.1007/s11340-020-00607-3>.
50. Yang, J. et al. SerialTrack: ScalE and Rotation Invariant Augmented Lagrangian particle tracking. *SoftwareX* **19**, 101204 (2022).

Table 1 Voice coil actuator (V-277.631) advanced tuning parameter set points for achieving peak impact rates

<i>V-277.631 Advanced Parameter</i>	<i>Set Point</i>
Position Axis Unit	mm
Position On Target Settling Time	0.010
Position On Target Tolerance	0.005
Position Range Limit Max	15.000
Position Range Limit Min	0.000
Position Report Offset	0.000
Position Report Scaling	0.500
Position Servo P-Term	8.500
Position Servo I-Term	0.150
Position Servo D-Term	0.005
Position Servo Inner Output Gain	1.500
Position Servo Static P-Term	8.000
Position Servo Static I-Term	0.004
Position Servo Static D-Term	0.005
Position Servo Static Inner Output Gain	1.500
Profile Generator Enable	On(1)
Profile Generator Maximum Acceleration	100000.000
Profile Generator Maximum Jerk	4000.000
Profile Generator Maximum Jounce	200000.000
Profile Generator Maximum Velocity	10000.000
Velocity Axis Unit	mm/s
Velocity On Target Setting Time	0.010
Velocity On Target Tolerance	20.000
Velocity Report Offset	0.000
Velocity Report Scaling	1.000
Velocity Servo P-Term	0.065
Velocity Servo I-Term	0.100
Velocity Servo D-Term	0.000
Velocity Servo Static P-Term	0.035
Velocity Servo Static I-Term	0.002
Velocity Servo Static D-Term	0.000

Table 2 Process parameters used for AL-DVC on polyacrylamide, AL-DIC on 2D PDMS, and AL-DIC on polyurethane Foam

<i>Parameter</i>	<i>AL-DVC Polyacrylamide</i>	<i>AL-DIC PDMS Substrate</i>	<i>AL-DIC Polyurethane Foam</i>
Experiment parameters			
Microscopy method	multi-photon $\lambda = 575/25$ nm	bright field	bright field
Imaging objective	40X (1.15 NA)	2X (0.06 NA)	2X (0.06 NA)
Pattern type / particle size	1 μm	speckle pattern	speckle pattern
Image size (px)	512 \times 2048 \times 281	1562 \times 1162	921 \times 708
Framerate, frames/s, (1/s)	Quasistatic	995	96
Post-processing parameters			
x & y μm -per-pixel conversion	0.41 $\frac{\mu\text{m}}{\text{px}}$	2.17 $\frac{\mu\text{m}}{\text{px}}$	3.25 $\frac{\mu\text{m}}{\text{px}}$
z -step size	1.1 μm		
Window Size (px)	64 \times 64 \times 32	20 \times 20	32 \times 32
Step Size (px)	64 \times 64 \times 32	10 \times 10	16 \times 16
Initial FFT Method	'bigxcorr'	Multigrid search	Multigrid search
Run mode (incremental or cumulative)	Inc	Cum.	Cum.

Table 3 HR-VPTM process parameters used for tension experiments in this study, and compared to the shear experiments in Buyukozturk et. al., 2022.

<i>Parameter</i>	<i>Tension Experiments</i>	<i>Shear Experiment [39]</i>
Experiment parameters		
Objective magnification, M_1 (Numerical aperture)	4X (0.2 NA)	4X (0.2 NA)
Relay magnification, M_2 Numerical aperture	4X (0.2 NA)	4X (0.13 NA)
Emission wavelength, λ (nm)	605	605
Particle size (μm)	10	15
Lenslet pitch, p_l (μm)	100	100
Microlens focal length, f_l (μm)	1000	1000
2D image size in x and y ($\text{px}_x \times \text{px}_y$)	$\approx 600 \times \approx 620$	$\approx 600 \times \approx 620$
Framerate, frames/s, (1/s)	200	1000
Volume reconstruction parameters		
μm -per-pixel conversion (x and y)	$1.64 \frac{\mu\text{m}}{\text{px}}$	$1.64 \frac{\mu\text{m}}{\text{px}}$
z-step size, z_s (μm)	5.0	5.0
z-range z_{min} to z_{max} (μm)	-650 to 65	-730 to 370
Lenslet pixel pitch, p_p (px)	15	15
Number of iterations, It_{num_1}	3	3
Lanczos filter width	2	2
Volume size, $S_x \times S_y \times S_z$ (px)	$791 \times 697 \times 144$	$791 \times 697 \times 221$
Post-processing parameters		
PSF bounding box size, BB_{size} (px)	$51 \times 51 \times \approx 105$	$51 \times 51 \times \approx 105$
Binarization threshold, Thr	0.01	0.08
Blob sizes, BS_{min} to BS_{max} (px^3)	100 to 10000	200 to 14000
Number of particles for PSF, N_{PSF}	1	2
Run mode (incremental or cumulative)	Inc	Inc
Deconvolution iterations, It_{num_2}	5	5
Outlier threshold	8	8
Global solver type	2	2
Regularization smoothness	0.05	0.03
Max number of neighbors	16	16